Fast simulation of complicated 3D structures above lossy magnetic media

Richard Y. Zhang, *Student Member, IEEE,* Jacob K. White, *Fellow, IEEE,*
and John G. Kassakian, *Life Fellow, IEEE*

Department of Electrical Engineering & Computer Science, Massachusetts Institute of Technology,
Cambridge MA, 02139, USA

A fast numerical method is presented for the simulation of complicated 3D structures, such as inductors constructed from litz or stranded wires, above or sandwiched between planar lossy magnetic media. Basing upon its smoothness, the quasistatic multilayer Green's function is numerically computed using finite differences, and its source height dependence is computed using an optimal Toeplitz-plus-Hankel decomposition. We show that a modified precorrected FFT method can be applied to reduce the dense linear algebra problem to near-linear time, and that frequency-dependent setups can be avoided to result in a considerable speed-up. Experimental verifications are made for a 16-strand litz wire coil, realistically modeled down to each individual strand. Results are obtained in 2-3 hours, showing an excellent agreement to measurements, and can be used to study the impact of transposition patterns in litz wire construction.

Index Terms—Numerical simulation, litz wire, magnetic multilayers, inductance, skin effect, integral equations

NOMENCLATURE

$\mathbf{r}$ Observation point located at (x, y, z).

$\mathbf{r}'$ Source point located at (x', y', z').

ρ Cylindrical radius of the vector $(\mathbf{r} - \mathbf{r}')$:
$\rho \equiv \sqrt{(x - x')^2 + (y - y')^2}$.

$[G]$ Multilayer Green's function. The brackets indicate that this is a second order tensor, i.e. a dyadic tensor.

G^{free} Free-space Laplacian Green's function; a scalar function defined in (9).

$[G^{add}]$ Additional Green's function component due to the presence of a multilayer; a dyadic tensor function defined in (8).

J_w The w-th component of $\mathbf{J}$, where $w \in \{x, y, z\}$.

$[A]$ The matrix or dyadic tensor named "A".

$A_{i,:}$ The i-th row of matrix $[A]$.

$A_{:,j}$ The j-th column of matrix $[A]$.

I. INTRODUCTION

MAGNETIC devices for power electronics are designed to maximize energy storage or transfer while minimizing losses. In applications where the geometry is approximately planar, the enhancement of energy storage is often achieved by placing the conductor coil on top or sandwiched between a magnetic multilayer media structure that serves as the magnetic core, as illustrated in Fig. 1. To minimize losses, the coil is often wound using some form of twisted, stranded or litz wire conductor pattern. Devices constructed in this way are common, and are found in applications such as planar monolithic inductors and transformers [1]–[3] and inductive power transfer systems [4]. Induction heating coils can also be viewed in this manner, and in these cases the multilayer
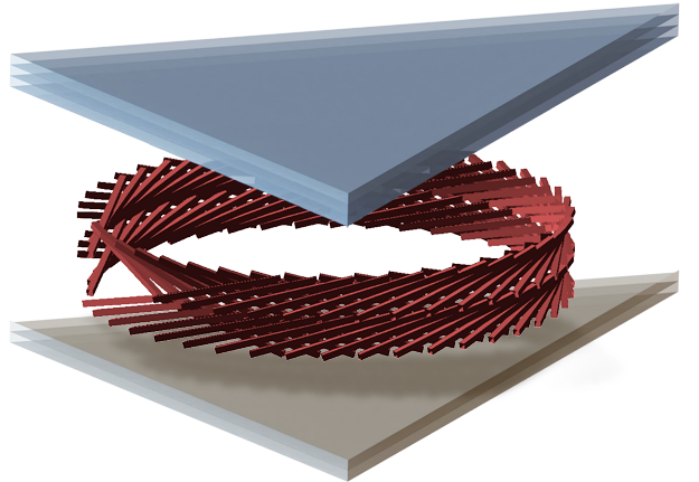
Figure 1: Illustration of the planar multilayer systems examined within this paper.

structure is a lossy-magnetic material that also serves as the load [5].

A fully three-dimensional numerical simulation of a litz wire coil, complete with realistic transposition patterns, is generally considered intractable even without the nearby multilayer media [6]–[8]. For coils in free-space, matches to experimental data can be achieved using a variety of simplified models, employing prior knowledge of the expected field and current density distributions, as well as symmetry between the strands in each bundle [6]–[9]. However, for lossy-magnetic multilayer structures, each strand of the coil experiences a proximity effect not only due to the nearby strands, but also due to the multilayer structure, complicating the overall analysis [7], [10].

In this paper, we present a general, numerical approach

to the litz-wire over lossy-magnetic structure problem. The objective is to realistically model the transposition pattern of the litz wire, and the interactions between the strands and the multilayer media, without making *a priori* assumptions about field and current distributions, and without heuristics that must be calibrated to experimental measurements. The issue of intractable complexity is reintroduced with a numerical approach, but we present a number of innovations in this paper that largely overcome this challenge.

Firstly, the method avoids discretizing the surrounding free-space and multilayer media, by the use of the multilayer Green's function [11]. This technique is widely used in microelectronic and microwave applications [12]–[15], but normally introduces a complicated Green's function that must be carefully evaluated with a Sommerfeld integral. In the quasistatic limit, we show in Section III that the Green's function is analytic smooth, and harmonic within free-space. Under these very special conditions, the Green's function can be directly evaluated to arbitrary accuracy using finite differences, a simple, well-established numerical technique that can be implemented with ease. Additionally, this finite differences approach also accommodates for continuous material variations in the $\hat{\mathbf{z}}$-direction.

However, the multilayer Green's function is translation-variant along $\hat{\mathbf{z}}$, and each finite differences solution is valid only for a single source point height z'. To minimize the number of finite differences solves needed to compute the full Green's function, and to put it in a form compatible with the FFT, we present in Section IV an optimal Toeplitz-plus-Hankel decomposition. By taking the values of the Green's function at just four carefully chosen source points z' as input, the decomposition is able to exactly reconstruct values of the Green's function at all other values of z'. Convolution with the multilayer Green's function can then be performed in $\mathcal{O}(n \log n)$ using the FFT.

Finally, we extend the smoothness property of the Green's function to frequency sweeps of the coil impedance. Normally, this procedure involves the use of a fast integral method (e.g. [16]–[19]), which compresses the governing system of linear equations and solves them iteratively. However, where the Green's function is frequency-dependent, the time-consuming setup must be repeated at each new frequency. In Section V we show that when the smooth quasistatic Green's function is applied to the precorrected FFT method [17], only one setup is needed for all frequencies. This leads to a speed advantage of more than five times when compared to the original pFFT algorithm in Section VIII.

In Section VI, we compare the accuracy of the numerical model to established analytical formulas. By reproducing the governing assumptions of the analytical models, results show that the numerical model is able to converge to 3 or more significant figures of accuracy.

Finally, in Section VII, we apply the method to a litz wire induction heating coil. We make measurements of all the characteristic dimensions of the coil, then construct a realistic model of the coil detailed down to each of its 16 individual strands, containing 909,504 individual elements. Predictions are made for the series inductance, resistance, and quality factor of the coil in free-space, and 11mm below a copper plate, computed on a workstation computer in 2-3 hours. The results show excellent agreement with measurements to experimental errors, and highlights the ability of the numerical method to fully account for the coupled interactions between the strands of the litz wire and the multilayer structure. By realistically modeling the woven structure of the litz wire, the simulation captures a number of subtle, geometry-sensitive characteristics that are missed by less detailed models.

II. FORMULATION

A. Governing Equations and Problem Geometry

In the presence of magnetic, conductive material, the electric field $\mathbf{E}$ is described by the *magnetic diffusion equation* [20]–[22]:

$$\nabla \times \frac{1}{\mu} \nabla \times \mathbf{E} = -j\omega(\sigma \mathbf{E} + \mathbf{J}^{exc}). \tag{1}$$

The formulation is constrained to inductive interactions in order to limit the degrees of freedom considered. It is assumed that capacitive displacement currents and charge accumulation are both second order:

$$j\omega\epsilon\mathbf{E} \approx 0, \quad \nabla \cdot \epsilon\mathbf{E} \approx 0. \tag{2}$$

The excitation current density, $\mathbf{J}^{exc}$, is due to current flow within the excitation conductors. As shown in Fig. 1, the conductors within this paper are positioned in a mostly planar fashion relative to the magnetic material layers, confined to a single layer of free-space denoted as Ω_0, but spaced away from the interface planes.

Beyond the free-space layer are an arbitrary number of layers, each with its own conductivity $\sigma(\mathbf{r})$, permeability $\mu(\mathbf{r})$, and permittivity $\epsilon(\mathbf{r}) = \epsilon_0$. We impose that the layer properties are constant over x and y such that translational invariance and isotropy can be established in these directions. No restrictions are imposed in the z direction; it is possible for each layer to have piecewise constant or continuously varying properties along z.

Substituting the quasistatic assumptions in (2) and expanding yields three equations for the three field components; for the two directions transpose to the layers, $w \in \{x, y\}$:

$$\nabla^2 E_w + \frac{1}{\mu}\frac{\partial\mu}{\partial z}\left(\frac{\partial E_w}{\partial z} - \frac{\partial E_w}{\partial w}\right) - j\omega\mu\sigma E_w$$
$$= j\omega\mu J_w^{exc}, \quad (3)$$

and for the direction normal to the layers, z:

$$\nabla^2 E_z - j\omega\mu\sigma E_z = j\omega\mu J_z^{exc}. \tag{4}$$

At discontinuous material interfaces where $\partial\mu/\partial z$ is unbounded, boundary conditions can be used:

$$\mathbf{E}|_{z=\zeta-} = \mathbf{E}|_{z=\zeta+}, \tag{5}$$

$$\frac{1}{\mu}\left(\frac{\partial E_w}{\partial z} - \frac{\partial E_z}{\partial w}\right)\Bigg|_{z=\zeta-} = \frac{1}{\mu}\left(\frac{\partial E_w}{\partial z} - \frac{\partial E_z}{\partial w}\right)\Bigg|_{z=\zeta+}. \tag{6}$$

Here, $z = \zeta$ is the interface plane.

B. Integral Equation Formulation

To obtain the electric field, $\mathbf{E}$, given a current excitation, $\mathbf{J}^{exc}$, the standard approach is to *solve* the governing equations (3)-(6) using the finite element method [23]–[25]. Alternatively, an integral equation formulation can be used to to *evaluate* $\mathbf{E}$ from $\mathbf{J}^{exc}$ directly, as in:

$$\mathbf{E}(\mathbf{r}) = -j\omega\mu_0 \int_{\Omega_C} \left[G(\mathbf{r},\mathbf{r}')\right] \mathbf{J}^{exc}(\mathbf{r}')\,\mathrm{d}\mathbf{r}', \qquad (7)$$

where the integration domain Ω_C is restricted to the support of the excitation current density.

Here, the Green's function dyadic tensor $\left[G\right]$ is the solution of (3)-(6) with a Dirac delta function excitation on the right hand side in each of the three Cartesian directions, and varies according to cylindrical radius, ρ, field point height, z and source point height, z'. We refer the reader to [15] for a thorough description of the general multilayer Green's functions method, and to [26], [27] for more accessible derivations specific to the lossy-magnetic problem.

For the remainder of this paper, we decompose the Green's function into a singular free-space component, and an additional component caused by the presence of the magnetic-conductive multilayer media:

$$\left[G(\mathbf{r},\mathbf{r}')\right] = \left[I\right] G^{free}(\mathbf{r},\mathbf{r}') + \left[G^{add}(\mathbf{r},\mathbf{r}')\right], \qquad (8)$$

where $\left[I\right]$ is the identity dyadic tensor, G^{free} is the singular, frequency-independent free-space Green's function:

$$G^{free}(\mathbf{r},\mathbf{r}') = \frac{1}{4\pi}\frac{1}{\|\mathbf{r}-\mathbf{r}'\|}, \qquad (9)$$

and $\left[G^{add}\right]$ is named the "added Green's function" for convenience. The separation of the singularity G^{free} from the Green's function is an important part of the formulation. As further explained throughout the remainder of this paper, the smoothness of $\left[G^{add}\right]$ in the source layer Ω_0 allows numerical methods based on Taylor polynomial expansions to be used, such as the finite differences method in Section III and the modified precorrected FFT method in Section V.

From (3)-(4), it readily follows that only the $\hat{\mathbf{x}}\hat{\mathbf{x}}$, $\hat{\mathbf{y}}\hat{\mathbf{y}}$, $\hat{\mathbf{z}}\hat{\mathbf{z}}$, $\hat{\mathbf{z}}\hat{\mathbf{x}}$ and $\hat{\mathbf{z}}\hat{\mathbf{y}}$ components of $\left[G^{add}\right]$ are non-zero:

$$\left[G^{add}\right] = \begin{bmatrix} G_{xx}^{add} & 0 & 0 \\ 0 & G_{yy}^{add} & 0 \\ G_{zx}^{add} & G_{zy}^{add} & G_{zz}^{add} \end{bmatrix}.$$

Technically, all five components of $\left[G^{add}\right]$ are needed to fully account for the presence of the multilayer media. However, if net current flow is overwhelmingly dominant in the transverse directions, then it can be assumed that $E_z \approx 0$ in the multilayer media. This sets the following three components to zero:

$$\{G_{zx}^{add}, G_{zy}^{add}, G_{zz}^{add}\} \approx 0, \qquad (10)$$

reducing the dyadic $\left[G^{add}\right]$ to a single scalar component, $G_{xx}^{add} = G_{yy}^{add}$. Substituting (8), (10) into (7) also reduces the dyadic integral of (7) into a scalar integral:

$$\mathbf{E}(\mathbf{r}) = -j\omega\mu_0 \int G^{free}(\mathbf{r},\mathbf{r}')\,\mathbf{J}^{exc}(\mathbf{r}')$$
$$+ G_{xx}^{add}(\mathbf{r},\mathbf{r}')\left(\hat{\mathbf{x}}J_x^{exc}(\mathbf{r}') + \hat{\mathbf{y}}J_y^{exc}(\mathbf{r}')\right)\mathrm{d}\mathbf{r}'. \qquad (11)$$

Hence, the ansatz in (10) provides a considerable reduction in complexity. For "almost-planar" problems, experimental experience suggest that (10) is an acceptable approximation [1], [3], [28]. Since the majority of multilayer problems have relatively flat geometries, the method presented within this paper was developed with (10) built in as an assumption. Experimental results presented in Section VII confirm that the prediction accuracy is not significantly affected for the geometries considered in this paper.

However, where current does not overwhelmingly flow transverse to the multilayer, e.g. in a vertically oriented coil, all five non-zero components of the dyadic $\left[G^{add}\right]$ must be carefully considered. These cases fall outside of the class of problems considered in this paper.

C. Field Evaluation via Conductor Discretization

For simple conductor geometries, evaluation of the electric field via (7) can sometimes be performed in closed form [1], [3], [28]. For more complicated geometries, the current density, $\mathbf{J}^{exc}$, is first discretized into the sum of n basis functions, as in:

$$\mathbf{J}^{exc}(\mathbf{r}) \approx \sum_{j=1}^{n} I_j \boldsymbol{\phi}_{\boldsymbol{j}}(\mathbf{r}). \qquad (12)$$

In this paper, we use rectangular, piecewise constant basis functions, $\boldsymbol{\phi}_{\boldsymbol{j}}$, defined as the following:

$$\boldsymbol{\phi}_{\boldsymbol{j}} = \begin{cases} \mathbf{u}_j/a_j & \mathbf{r} \in U_j \\ 0 & \mathbf{r} \notin U_j \end{cases}, \qquad (13)$$

where the support of the function, U_j, is a rectangular parallelepiped pointing in the direction along the unit vector $\mathbf{u}_j$, with cross-sectional area a_j. Physically, each basis function can be interpreted as a brick-shaped conductor filament, with a constant current density that flows along its length. The vector of discretized values, $I_b = [I_1, I_2, \ldots, I_n]^T$, describes the currents flowing through each of the n filaments that discretize $\mathbf{J}^{exc}$. This vector is also referred to as the *branch currents*.

The primary advantage of discretization using brick-shaped filaments is the closed-form solutions to the singular free-space mutual inductance integral of (21), which can be found in [29], [30]. Clearly, the disadvantage is the "staircase effect" when attempting to model smoothly varying current densities and current redistribution effects. The staircase effect can be mitigated by refining conductor segments along their cross-sections [31]. It is often helpful to allocate more sub-conductors closer to the conductor surface, for example according to a cosine rule, as shown in Fig. 2.

Once $\mathbf{J}^{exc}$ is discretized, the electric field is obtained by computing the contributions of each basis function via (7), and summing the results together. Substituting (12), (13) into (7) yields:

$$\mathbf{E}(\mathbf{r}) = -j\omega\mu_0 \sum_{j=1}^{n} \frac{I_j}{a_j} \int_{U_j} \left[G(\mathbf{r},\mathbf{r}')\right]\mathbf{u}_j\,\mathrm{d}\mathbf{r}', \qquad (14)$$

which becomes a matrix-vector product when evaluated at specific observation points. For example, let $E_w =$
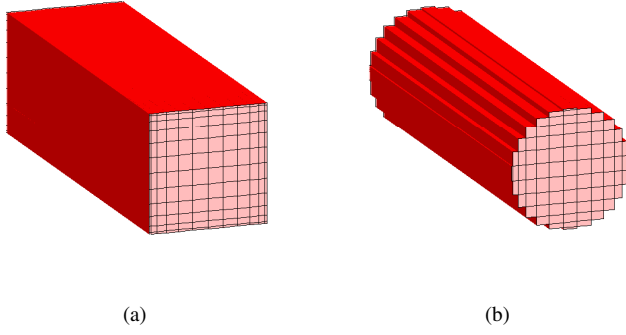
Figure 2: Refinement of a conductor to simulate high-frequency current redistribution effects and non-orthogonal geometries. (a) Division of a square cross-section using a cosine rule. (b) Example model of a circular cross-section.

$[E_w^{(1)}, E_w^{(2)}, \ldots, E_w^{(m)}]^T$ be the vector of $\hat{\mathbf{w}}$-directional electric fields evaluated at the observation points, $\mathbf{p}_i : i \in [1, m]$. For each observation point, we have:

$$E_w^{(i)} = \hat{\mathbf{w}} \cdot \mathbf{E}(\mathbf{p}_i) = \sum_{j=1}^{n} \Psi_{i,j} I_j, \qquad (15)$$

where element (i, j) of the matrix $[\Psi] \in \mathbb{C}^{m \times n}$ contains the field contributions in the $\hat{\mathbf{w}}$-direction made by the j-th basis function, towards the i-th observation point:

$$\Psi_{i,j} = \hat{\mathbf{w}} \cdot \left(\frac{-j\omega\mu_0}{a_j} \int_{U_j} [G(\mathbf{p}_i, \mathbf{r}')] \, \mathbf{u}_j \, \mathrm{d}\mathbf{r}' \right). \qquad (16)$$

D. Impedance Extraction using the PEEC method

Impedance extraction is an inverse problem that solves conductor current densities for a specified voltage difference at the terminals. Impedance extraction can be accomplished by the Partial Element Equivalent Circuit (PEEC) method [32], which reformulates the electromagnetic interactions into a circuit network model.

To begin, a voltage-drop is defined for each brick-shaped filament, by integrating and averaging the electric field over each basis function:

$$V_i = -\int \boldsymbol{\phi}_i(\mathbf{r}) \cdot \mathbf{E}(\mathbf{r}) \, \mathrm{d}\mathbf{r} = \frac{-1}{a_i} \int_{U_i} \mathbf{u}_i \cdot \mathbf{E}(\mathbf{r}) \, \mathrm{d}\mathbf{r}. \qquad (17)$$

The resulting vector of discretized values, $V_b = [V_1, V_2, \ldots, V_n]^T$, is referred to as the *branch voltages* vector.

Substituting the electric field superposition integral (14) into (17) forms a dense impedance matrix, $[Z] \in \mathbb{C}^{n \times n}$, that relates branch currents to branch voltages:

$$V_b = \{[R] + j\omega[L]\} I_b = [Z] I_b, \qquad (18)$$

where $[R]$ is the diagonal branch resistance matrix, and $[L]$ is the dense self and mutual branch inductance matrix:

$$L_{ij} = \mu_0 \int_{U_i} \frac{\mathbf{u}_i}{a_i} \cdot \left(\int_{U_j} [G(\mathbf{r}, \mathbf{r}')] \, \frac{\mathbf{u}_j}{a_j} \, \mathrm{d}\mathbf{r}' \right) \, \mathrm{d}\mathbf{r}, \qquad (19)$$

also referred in literature as the partial inductances matrix [32], [33]. Substituting (11) as an expansion for (7) into (19) yields:

$$L_{ij} = L_{ij}^{free} + L_{ij}^{add} \qquad (20)$$

where

$$L_{ij}^{free} = C \frac{\mu_0}{a_i a_j} \int_{U_j} \int_{U_i} G^{free}(\mathbf{r}, \mathbf{r}) \, \mathrm{d}\mathbf{r}' \, \mathrm{d}\mathbf{r}, \qquad (21)$$

$$L_{ij}^{add} = D \frac{\mu_0}{a_i a_j} \int_{U_j} \int_{U_i} G_{xx}^{add}(\mathbf{r}, \mathbf{r}') \, \mathrm{d}\mathbf{r}' \, \mathrm{d}\mathbf{r}, \qquad (22)$$

and the constants C and D are:

$$C = \mathbf{u}_i \cdot \mathbf{u}_j, \quad D = u_{i,x} u_{j,x} + u_{i,y} u_{j,y}.$$

The singular integral (21) for the free-space mutual inductance L_{ij}^{free} has closed-form solutions when the brick-shaped filaments U_i and U_j are parallel along their edges in the "Manhattan geometry" [30]. In non-Manhattan cases, the surface-to-surface procedure described in Appendix A can be used to evaluate (21) to arbitrary precision. The explicit evaluation of the additional inductance L_{ij}^{add} can be avoided altogether by the use of the precorrected FFT algorithm, as discussed later in Section V.

The circuit model described in (18) is incomplete without the specification of Kirchhoff's voltage and current laws. As noted in [34], these constraints can be enforced by introducing the mesh-analysis matrix, $[M] \in \mathbb{R}^{n \times l}$, which maps n branches to l closed loops of current (known as meshes) with order l non-zero entries:

$$[M]^T I_m = I_b, \qquad (23)$$

$$V_m = [M] V_b. \qquad (24)$$

Here, $V_m, I_m \in \mathbb{R}^{l \times 1}$ are known as the mesh loop voltage and current vectors. Substituting (23),(24) into (18) yields:

$$[M][Z][M]^T I_m = V_m, \qquad (25)$$

where the right-hand side V_m is zero everywhere except those rows corresponding to terminal voltage excitations. Solving (25) gives the terminal admittances at the corresponding rows of I_m, concluding the impedance extraction procedure.

For large problems where a direct matrix inversion is prohibitively complex, (25) can be efficiently solved using Krylov subspace iterative methods such as GMRES [35], coupled with a suitable preconditioner. Iterative Krylov methods require many dense matrix-vector products in (18), but these can be performed in $\mathcal{O}(n)$ or $\mathcal{O}(n \log n)$ complexity using fast integral methods such as the fast multipole method [16], the precorrected FFT [17], hierarchical-SVD [18] and adaptive cross-approximation methods [19]. The interested reader is referred to [34] for a detailed description of solving (25) using GMRES and a series of fast matrix vector products.

E. Matrix-vector product acceleration with the pFFT

The precorrected FFT (pFFT) is a fast method that implicitly forms dense matrices, such as $[Z]$ in (18), and $[\Phi]$ in (15), as a summation of sparse components, and evaluates matrix-vector products with them in $\mathcal{O}(n \log n)$ complexity. As a fast method, its asymptotic complexity is higher than $\mathcal{O}(n)$; however, for integral equations evaluated over approximately homogenous volumes, it is known to be considerably more efficient than competing methods [36]. Furthermore, as discussed in detail in Section V, pFFT allows an efficient treatment of a smooth multilayer Green's function over many frequencies with very little additional overhead.

The pFFT algorithm is well-known in [17], [36], [37], and an application-specific summary is provided here for completeness. Given a dense matrix, $[A]$, the pFFT algorithm approximates the matrix using a sum and products of sparse matrices:

$$[A] = [S] + [I][H][P], \qquad (26)$$

where $[S]$ represents nearby interactions, and $[I][H][P]$ represents distant interactions. More specifically, each matrix in (26) is a step in the algorithm:

1) Projection matrix $[P]_{m \times n}$: Represents the integration over n basis functions $\phi_j : j \in [1, n]$ as equivalent weighted point sources on a regular grid of m points. The basis function to grid projection is performed either using a collocation scheme [17], [36] or a polynomial interpolation scheme [37], [38].

2) Convolution matrix $[H]_{m \times m}$: convolves the grid of m weighted point sources with the governing Green's function using the FFT, to produce potentials evaluated on the m grid points.

3) Interpolation matrix $[I]_{n \times m}$: Interpolates the m grid evaluations onto the desired evaluation points or basis functions, again with either collocation or polynomial interpolation.

4) Precorrected direct matrix $[S]_{n \times n}$: computes self- and nearby interactions directly, and corrects for the inaccurate contributions from the grid.

The sparse $[S]$ matrix is computed once per problem and per Green's function, but it is none-the-less the most expensive part of the algorithm. For each neighboring pair of basis functions with indices i and j, the precorrected direct term $S_{i,j}$ is written:

$$S_{i,j} = A_{i,j} - I_{i,:}[H]P_{:,j},$$

where $A_{i,j}$ is the (i, j)-th element of the original dense matrix $[A]$, representing the direct interaction between the pair, and $I_{i,:}[H]P_{:,j}$ is the precorrection, calculated by performing the projection-convolution-interpolation procedure using the j-th column of $[P]$ and the i-th row of $[I]$. The precorrection step is necessary because most electromagnetic field Green's functions are singular at $\mathbf{r} = \mathbf{r}'$, making grid-based projection and interpolation inaccurate for near-by interactions. Once the $[S]$ matrix is formed, multiplication operations with it are inexpensive and add relatively little overhead to each matrix-vector product operation.

III. THE MULTILAYER GREEN'S FUNCTION

Existing multilayer media Green's function field solvers can be grouped into two broad categories based on the applications. Where the conductor geometries are complicated, for example in microstrip circuits and VLSI interconnects applications, the Green's functions tend to be simple. The usual practice is to analytically derive and compute the Green's function, and to focus efforts on reducing complexity in the conductors [3], [12], [39], [40]. By contrast, for antennas and scattering applications, the Green's functions themselves contain a great deal of complexity, including resonant and propagation modes, surface waves, and branch cuts in the complex domain, and most of the emphasis is placed upon evaluating the Green's function to high accuracy using sophisticated techniques [13]–[15].

The lossy magnetic multilayer media problem shares characteristics with both classes of problems. On one hand, the conductors can contain complicated geometric details, such twisted and interwoven wire patterns, motivating the adaptation of fast integral equation techniques. But on the other hand, the multilayers themselves also tend to be complex. For example, in the induction heating of iron and steel alloys, magnetic field penetration into the layered media may cause orders of magnitude of continuous variation in the linearized magnetic permeability and conductivity along the z direction [41].

In this section, we describe a simple procedure to evaluate the multilayer Green's function numerically, using nonuniform finite differences in the spatial domain. In addition to the obvious appeal of simplicity, the finite differences approach can readily accommodate continuous material variations, which is a difficult task to accomplish using piecewise constant analytical techniques. Furthermore, error control is easily implemented using standard finite differences adaptive meshing techniques, and convergence is guaranteed due to the smoothness of the underlying solution. While the approach cannot be easily extended to the general full-wave problem due to wave reflections at the outer boundaries [42], [43], we show in this section that it is efficient and competitive for the types of layered problems considered within this paper.

A. Quasistatic Added Green's Function

Under the quasistatic limit, the added Green's function G_{xx}^{add} is piecewise infinitely differentiable smooth (i.e. piecewise C^{∞}). This smoothness property is an important theme for this paper, because it is the key factor that allows numerical methods based on Taylor polynomial expansions to be effective, including the finite differences method described below, and the polynomial projection operation in the pFFT in Section V. In the following subsection, we provide a brief sketch to illustrate the smoothness property, and the implied existence and uniqueness of the solution.

Following the naming conventions illustrated in Fig. 3, let the open domain of free-space containing the conductors be denoted as $\Omega_0 \subset \mathbb{R}^3$, and consider solving for the $\hat{\mathbf{x}}\hat{\mathbf{x}}$ component of $[G]$ in (1). This yields Laplace's equation:

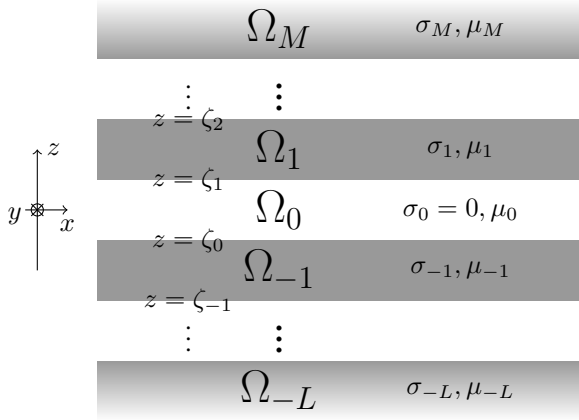$$\nabla^2 G_{xx} = -\delta(\mathbf{r}), \quad \mathbf{r} \in \Omega_0.$$

Figure 3: Notations to describe a general multilayer geometry.

Consequently, the solution G_{xx} is harmonic within the region Ω_0. Since G^{free} is harmonic in $\mathbb{R}^3$ by definition, $G_{xx}^{add} = G_{xx} - G^{free}$ must also be harmonic within Ω_0. Additionally, with the source singularity canceled out, G_{xx}^{add} is also smooth at its origin. Due to the strong maximum principle for harmonic functions, G_{xx}^{add} must attain its maximum and minimum along the boundaries $\partial\Omega_0$.

Outside the source layer Ω_0, G_{xx}^{add} remains smooth within each domain. Let Ω_i denote the domain of the i-th piecewise layer of the multilayer media. Within each Ω_i, equation (1) can be written in a linear differential operator form:

$$Lu(\mathbf{r}) = \left(\nabla^2 + a(\mathbf{r})\frac{\partial}{\partial z} - b(\mathbf{r})\right)u(\mathbf{r}) = 0, \quad \mathbf{r}\in\Omega_i,$$

where $u(\mathbf{r})$ represents the homogenous solution, and corresponds to the value of G_{xx}^{add} within that domain. The linear operator L is a perturbed version of the Laplacian, and is therefore elliptic. If the material properties μ and σ in each layer are bounded and analytic, then the coefficients a and b are also bounded and analytic. In this case, the regularity of elliptic operators guarantees that the solution, u, will also be analytic and infinitely differentiable within Ω_i [44, p.178].

To connect the solutions in each domain, we note that the global solution must be Lipschitz continuous, since the the boundary conditions (5)-(6) are equivalent to a description of local Lipschitz continuity for finite values of μ, and the solution is infinitely differentiable elsewhere. Then, by applying the Picard–Lindelöf theorem along the z direction for each fixed ρ (see [45], [46]), there exists a unique solution to the boundary value problem, and that solution is bounded everywhere except at the origin where the excitation may be singular.

B. Finite Differences Evaluation of the Green's function

Consider the geometry shown in Fig. 3. At the center of the geometry is the layer Ω_0 containing the point source, with conductivity $\sigma_0 = 0$ and permeability μ_0. Above and below Ω_0 are M and L layers of magnetic conductive materials, each containing its own conductivity σ_k and permeability μ_k that may be variable along z. For each each layer Ω_k, label the height of the boundary directly below it as $z = \zeta_k$.

The transverse Green's function $G_{xx}(\mathbf{r},\mathbf{r}')$ is obtained by solving (3) with an $\hat{\mathbf{x}}$-directed delta excitation located at a height of z', for the electric field in the $\hat{\mathbf{x}}$-direction $E_x(\mathbf{r})$. We begin by setting $\mathbf{J}^{exc}$ to the following:

$$-j\omega\mu_0 J_x^{exc} = \delta(x)\delta(y)\delta(z-z'),$$
$$J_y^{exc} = J_z^{exc} = 0. \tag{27}$$

Substituting (27) into (3) yields one governing equation for each layer of material:

$$\nabla^2 E_x = -\delta(x)\delta(y)\delta(z-z') \qquad \zeta_0 \le z \le \zeta_1 \tag{28}$$
$$\left(\nabla^2 + \frac{1}{\mu^2}\frac{\partial\mu}{\partial z}\frac{\partial}{\partial z} - j\omega\mu\sigma\right)E_x = 0 \qquad \text{otherwise} \tag{29}$$

Equations (28) and (29) are cylindrically symmetric, and the Laplacian operator can be expanded to its cylindrically symmetric form:

$$\nabla^2 \equiv \frac{1}{\rho}\frac{\partial}{\partial\rho} + \frac{\partial^2}{\partial\rho^2} + \frac{\partial^2}{\partial z^2}. \tag{30}$$

Let the $\hat{\mathbf{x}}$-directed electric field within each region Ω_k be labeled with superscripts as $E_x^{(k)} \equiv \{E_x(\mathbf{r}) : \mathbf{r}\in\Omega_k\}$. Using this notation, the interface boundary between each neighboring layer pairs $E_x^{(k)}$ and $E_x^{(k-1)}$ are written:

$$E_x^{(k)} - E_x^{(k-1)} = 0 \qquad z = \zeta_k, \tag{31}$$
$$\frac{1}{\mu_k}\frac{\partial}{\partial z}E_x^{(k)} - \frac{1}{\mu_{k-1}}\frac{\partial}{\partial z}E_x^{(k-1)} = 0 \qquad z = \zeta_k, \tag{32}$$

corresponding respectively to the continuity of the tangential electric fields $\hat{\mathbf{x}}E_x$ and tangential magnetic fields $\hat{\mathbf{y}}H_y = (\nabla\times\hat{\mathbf{x}}E_x)/\mu$.

The singularity on the right-hand side of (28) is a discontinuity that poses an issue for finite differences. However by the field equivalence principle, it can be eliminated and replaced with surface magnetic and electric currents at the boundaries of Ω_0 [11]. First, we note that (28) is Laplace's equation within the source layer Ω_0, and the source contribution is equal to $G^{free}(\mathbf{r},\mathbf{r}')$, defined earlier in (9). Subtracting the source contribution leaves the homogenous equation in that layer:

$$\nabla^2 E_{hom} = 0 \qquad \zeta_0 \le z \le \zeta_1, \tag{33}$$

where,

$$E_{hom} = E_x^{(0)} - G^{free}(\mathbf{r},\mathbf{r}'). \tag{34}$$

Note that E_{hom} corresponds to the added Green's function component G_{xx}^{add} within the layer Ω_0.

The equivalent magnetic and electric surface currents to replace the original point excitation are placed at the boundaries of layer Ω_0. Their strengths can be computed by substituting (34) for E_{hom} back into the regular boundary conditions (31),(32). At the boundary above Ω_0 we have:

$$E_x^{(1)} - E_{hom} = G^{free} \qquad z = \zeta_1, \tag{35}$$
$$\frac{\mu_0}{\mu_1}\frac{\partial}{\partial z}E_x^{(1)} - \frac{\partial}{\partial z}E_{hom} = \frac{\partial}{\partial z}G^{free} \qquad z = \zeta_1, \tag{36}$$

and at the boundary below Ω_0:

$$E_x^{(-1)} - E_{hom} = G^{free} \qquad z = \zeta_0, \tag{37}$$

$$\frac{\mu_0}{\mu_{-1}} \frac{\partial}{\partial z} E_x^{(-1)} - \frac{\partial}{\partial z} E_{hom} = \frac{\partial}{\partial z} G^{free} \qquad z = \zeta_0, \tag{38}$$

where G^{free} and $\partial G^{free}/\partial z$ expand to the following form in cylindrical coordinates:

$$G^{free} = \frac{1}{4\pi \left[\rho^2 + (z - z')^2\right]^{1/2}}, \tag{39}$$

$$\frac{\partial}{\partial z} G^{free} = \frac{-(z - z')}{4\pi \left[\rho^2 + (z - z')^2\right]^{3/2}}. \tag{40}$$

Given a fixed value of z', equations (31)-(38) combine to form a two-dimensional boundary value problem for $E_{hom}(\rho, z) \equiv G_{xx}^{add}(\rho, z; z')$ in region Ω_0, and for $E_x^{(k)}(\rho, z) \equiv G_{xx}(\rho, z; z')$ outside of Ω_0. The homogenous equations, (33) and (29), govern the domains, and the boundary conditions, (31) and (32), govern all regular interfaces. The impulse excitation of (28) is replaced by boundary magnetic and electric currents, (35)-(38), located at the excited interfaces at $z = \zeta_1$ and $z = \zeta_0$. These surface currents are smooth and non-singular, so long as the source point $\mathbf{r}'$ is not held exactly on top of the surfaces.

To solve these equations, the spatial derivative operators (30) can be discretized using non-uniform finite differences techniques, the details of which are available in many reference texts [47], [48]. In practice, the authors have found this approach to be competitive in problems where only 3-4 significant figures of accuracy are desired. To illustrate, the degrees of freedom needed to achieve $\sim 0.1\%$ accuracy is around 100,000 for the cases considered in Sections VI and VII. The associated linear systems are directly inverted in MATLAB on a 2.5 GHz dual-core CPU in less than 10 seconds.

If more significant figures are desired, then the Hankel transform can be used to transform the spatial radial direction ρ to its spectral domain. The difficulties associated with Sommerfeld integrals are reintroduced with this approach, and the reader is referred to [42], [43] for more details.

IV. DECOUPLING THE Z-DIRECTIONAL DEPENDENCE

When the multilayer Green's function is computed numerically using the finite differences method described above, only one "slice" of G_{xx}^{add} is computed at a time, for all values of ρ and z, but a single fixed value of z'. To avoid repeating the finite differences solve for a range of z', this section describes a method that performs the following method-of-images decomposition:

$$G_{xx}^{add}(\rho, z, z') = T(\rho, z - z') + H(\rho, z + z'). \tag{41}$$

This linear algebra method, named the Toeplitz-plus-Hankel decomposition due to the underlying matrix structure, reconstructs the least-squares values of T and H from the values of G_{xx}^{add} evaluated at just four carefully chosen source points z'. The resultant components can exactly recreate the values of G_{xx}^{add} for all values of z', despite sampling it at only four distinct slices.

Furthermore, it is well-known that multilayer Green's functions are not translation-invariant along the $\hat{\mathbf{z}}$-direction, and cannot be directly convolved along this direction using the FFT. Instead, the two components T and H can be separately convolved using the FFT. The T component is treated like a regular three-dimensional convolution, and the H component is treated as a convolution along $\hat{\mathbf{x}}$ and $\hat{\mathbf{y}}$, and a cross-correlation along $\hat{\mathbf{z}}$. In fact, previous authors have found that the two-component convolution above incurs relatively little overhead when compared to the traditional single-component convolution for translation-invariant Green's functions [12], [36].

A. Toeplitz-plus-Hankel Decomposition

Consider discretizing (41) to a matrix $[\Psi]$ for a uniformly sampled $z_i : i \in [1, N]$ and a fixed value $\rho = \rho_0$:

$$\Psi_{i,j} = G_{xx}^{add}(\rho = \rho_0, z = z_i, z' = z_j). \tag{42}$$

If the vectors $t, h \in \mathbb{C}^{2N-1 \times 1}$ are defined using the functions T and H from (41):

$$t_{i-j} = T(\rho_0, z_i - z_j), \quad h_{i+j} = H(\rho_0, z_i + z_j),$$

then all N^2 elements of $[\Psi]$ can be expressed in terms of t and h, in a *Toeplitz-plus-Hankel* structure:

$$\Psi_{i,j} = t_{i-j} + h_{i+j}. \tag{43}$$

Equation (43) can be expressed as a system of linear equations:

$$[B] \begin{bmatrix} t_{1-n} \\ \vdots \\ t_0 \\ \vdots \\ t_{n-1} \end{bmatrix} + [C] \begin{bmatrix} h_2 \\ h_3 \\ \vdots \\ h_{2n-1} \\ h_{2n} \end{bmatrix} = \begin{bmatrix} \Psi_{1,1} \\ \Psi_{2,1} \\ \vdots \\ \Psi_{n-1,n} \\ \Psi_{n,n} \end{bmatrix}$$

$$[B]t + [C]h = \psi, \tag{44}$$

$$[A] \begin{bmatrix} t \\ h \end{bmatrix} = \psi. \tag{45}$$

where the vector $\psi \in \mathbb{C}^{N^2 \times 1}$ is the column vectorization of the matrix $[\Psi]$:

$$g = \text{vec}([\Psi]).$$

The matrices $[B], [C] \in \mathbb{R}^{N^2 \times 2N-1}$ are sparse coefficient matrices of ones and zeros, and the matrix $[A] \in \mathbb{R}^{N^2 \times 4N-2}$ is the horizontal concatenation of $[B]$ and $[C]$. Consider partitioning $[A]$ into N blocks of N rows each, and referring to each block using subscripts:

$$A = \begin{bmatrix} A_1 \\ A_2 \\ \vdots \\ A_N \end{bmatrix},$$

then observing (43), each i-th block of A can be shown to have the following sparsity pattern for an ascending ordering of t and h:

$$A_i = \begin{bmatrix} 0_{N \times N-i} & I_N & 0_{N \times 2i-2} & I_N & 0_{N \times i-1} \end{bmatrix}. \tag{46}$$

Matrix $[A]$ is greatly overdetermined, possessing N^2 equations for just $4N-2$ unknowns. Assuming that $[\Psi]$ does indeed contain a Toeplitz-plus-Hankel structure, then $[A]$ is reducible to just four of its blocks while preserving the integrity of the decomposition. Let the reduced form of $[A]$ formed by isolating blocks a, b, c, d be denoted $[D]$:

$$\begin{bmatrix} A_a \\ A_b \\ A_c \\ A_d \end{bmatrix} \begin{bmatrix} t \\ h \end{bmatrix} = [D] \begin{bmatrix} t \\ h \end{bmatrix} = \psi^*, \qquad (47)$$

where ψ^* is the column vectorization of the a-th, b-th, c-th and d-th columns of matrix $[\Psi]$:

$$\psi^* = \mathrm{vec}(\begin{bmatrix} \Psi_{:,a} & \Psi_{:,b} & \Psi_{:,c} & \Psi_{:,d} \end{bmatrix}). \qquad (48)$$

Solving the matrix equation (47) completes the Toeplitz-plus-Hankel decomposition.

The appropriate choice for a, b, c, d can be readily verified by forming the full $[A]$ matrix, selecting specific blocks to form $[D]$, and checking to see that both matrices maintain the same rank. For even values of N, the following choices have been experimentally found to be optimal:

$$a = 1, \qquad b = N, \qquad (49)$$

$$c = \mathrm{round}(1.6 \log N), \quad d = c + \frac{N}{2}, \qquad (50)$$

where $\log$ is the natural logarithm. A formal proof of these results involves an in-depth analysis into the sparsity structure of $[A]$ using elements of spectral graph theory, and can be found in a separate upcoming paper.

V. FAST FREQUENCY SWEEPS

As described in Section II, fast integral methods (e.g. [16]–[19]) implicitly form the coupling matrix–$[\Phi]$ in (15) and $[Z]$ in (18)–in a compressed structure, and perform fast matrix-vector products directly with the compressed structure. The initial setup is geometry dependent and Green's function dependent, and it is always time-consuming, taking several tens to thousands of times the cost of each subsequent matrix-vector product. Where the Green's function is fixed for all frequencies, e.g. in free-space impedance extraction, the initial setup is performed just once for each conductor geometry. However, when extended to multilayer Green's functions, repeating the setup at each new frequency adds a considerable computational overhead.

Instead, we show in this section that the smoothness of the quasistatic added Green's function G_{xx}^{add} in Ω_0 (as previously shown in Section III) allows the initial setup to be performed just once per geometry, regardless of its frequency-dependence. This completely eliminates the overhead associated with repeating the setup at each frequency, resulting in a considerable speedup.

Consider the convolution and precorrection matrices $[H]$ and $[S]$ in the pFFT equation (26), which are both frequency-dependent. Let this frequency-dependence be denoted with the function argument f:

$$[A(f)] = [S(f)] + [I][H(f)][P], \qquad (51)$$

Following (8), the coupling matrix $[A]$ can be decomposed according to contributions due to G^{free} and those due to G_{xx}^{add}:

$$[A(f)] = [A^{free}] + [A^{add}(f)]. \qquad (52)$$

This leads to similar decomposition for the frequency dependent matrices $[S(f)]$ and $[H(f)]$:

$$[S(f)] = [S^{free}] + [S^{add}(f)] \qquad (53)$$

$$[H(f)] = [H^{free}] + [H^{add}(f)]. \qquad (54)$$

Note that only the added components of each matrix is frequency-dependent.

In Section III, it was shown that a finite differences discretization of G_{xx}^{add}–based upon approximating the underlying solution with a truncated Taylor polynomial series [48]–will converge to arbitrary accuracy as the grid size is refined. We emphasize here that the projection and interpolation operations in our FFT are also based upon approximating the underlying solution with a truncated Taylor polynomial series (see [37] for a more thorough description of these operations). Consequently, we expect the pFFT method without precorrection to also become increasingly accurate as the FFT grid is refined. Substituting into (51) and (52), this observation can be written as a limit statement, for an FFT grid spacing of h:

$$\lim_{h \to 0} [I][H^{add}(f)][P] = [A^{add}(f)], \qquad (55)$$

noting the absence of the precorrection matrix $[S^{add}(f)]$.

Equivalently, the free-space, frequency-independent precorrection matrix $[S^{free}]$ becomes a better approximation for the overall precorrection matrix $[S]$ with a refinement of the grid:

$$\lim_{h \to 0} [A(f)] = [S^{free}] + [I][H(f)][P], \qquad (56)$$

where unlike before in (51), the $[S^{free}(f)]$ term has been dropped from the equation.

Equation (56) summarizes the fast version of pFFT for quasistatic multilayer Green's functions. For some well-chosen value of h, the frequency-independent matrix $[S^{free}]$ becomes an accurate approximation for the frequency-dependent matrix $[S(f)]$. At each new frequency, the projection-convolution-interpolation part of pFFT is performed using the full, frequency-dependent convolution matrix $[H(f)]$, but the pre-correction is performed using the frequency-independent $[S^{free}]$.

While this may appear to be a trivial adaptation of the full pFFT method, it has significant ramifications for the speed of frequency sweeps. The most time-consuming step of pFFT–the formation of the precorrection matrix–is performed just once for all frequencies, rather than repeated at each frequency. The need to form $[S^{add}(f)]$ is eliminated altogether, and this provides an advantage in itself, because each of its elements is the end-result of an expensive six-dimensional integral, shown in (22).

To control errors to some specified limit, the exact value of grid refinement h for (56) may be numerically estimated by explicitly forming $[S^{add}(f)]$ to within a relative error tolerance ϵ:

$$\|[S^{add}(f)]\| \leq \epsilon \|[S^{free}]\|, \qquad (57)$$

```
1: procedure EXTRACTIMP(geometries, frequencies)
2:    %Begin pFFT setup.
3:    [P], [I] ← Project conductors onto a uniform grid.
4:    [S_free] ← Precorrect G^free(ρ, z, z')         ▷ slow!
5:    [S_free] ← Compute direct interactions         ▷ slow!
6:    for each frequency do
7:       %Set up convolution components for each
8:       %frequency w/o precorrecting again.
9:       G^add ← Load added Green's function.
10:      G ← G^add + G^free        ▷ add free-space component
11:      %Begin GMRES interations
12:      V = [1, 0, 0....] ▷ Objective is 1 volt across terminals
13:      while Ṽ not converged to V do
14:         Guess new current density x using GMRES
15:         %Perform matrix-vector product
16:         x_p = [P]x                              ▷ Project
17:         E ← CONVOLVE(x_p; G)
18:         %E is the E-field evaluated on a grid
19:         Ṽ = [I]E + [S_free]x  ▷ Interpolate and Precorrect
20:      end while
21:      Z(f) = 1/I              ▷ Compute terminal impedance
22:   end for
23: end procedure
```

Figure 4: The full impedance extraction procedure in pseudocode. Highlighted are the aspects of the algorithm accelerated by pFFT and by the G^{add} decomposition.

under a preferred norm.

A summary of a frequency-sweep impedance extraction routine based upon the fast frequency sweep described above is shown in Fig. 4 in pseudocode. Experimental confirmation of the fast pFFT method is presented below in Table II.

VI. COMPARISON TO ANALYTICAL MODELS

A wealth of analytical models have been previously derived for the lossy-magnetic coil problem, many of which are exact under specific conditions and for particular conductor geometries. In this section we demonstrate the ability of our numerical model to converge towards a few of the most widely used exact solutions in inductor design, when their relevant conditions are reproduced.
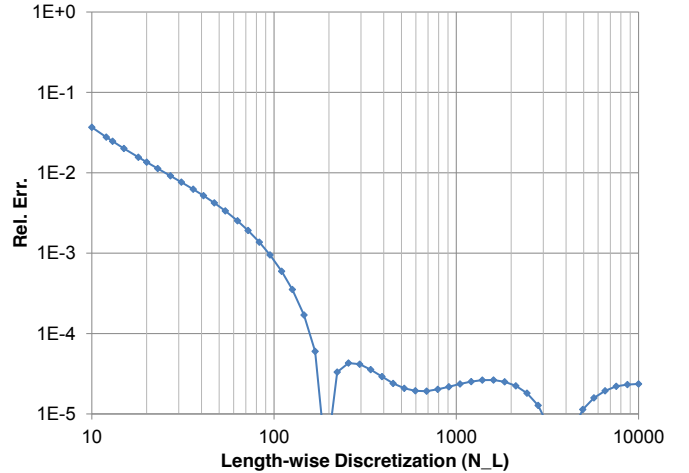
A. Inductance of a single turn in free-space

The exact self-inductance for a circular turn of wire in free-space can be derived when the cross-section of the wire is rectangular or square and the current density is assumed to be constant [29], [49]. Consider a single circular turn of radius 0.1m, with a square cross-section of 1mm in width and height. Using equations (91) and (92) from [29, pp.95], the exact self-inductance of this single turn evaluates to 689.859nH, with 4-5 s.f. of accuracy.

The circular turn is numerically modeled as an N_L-sided polygon, with a single piecewise-constant rectangular parallelepiped basis function as its cross-section. The convergence of the self-inductance with increasing N_L are plotted in Fig. 5, computed using the method described in this paper. Results
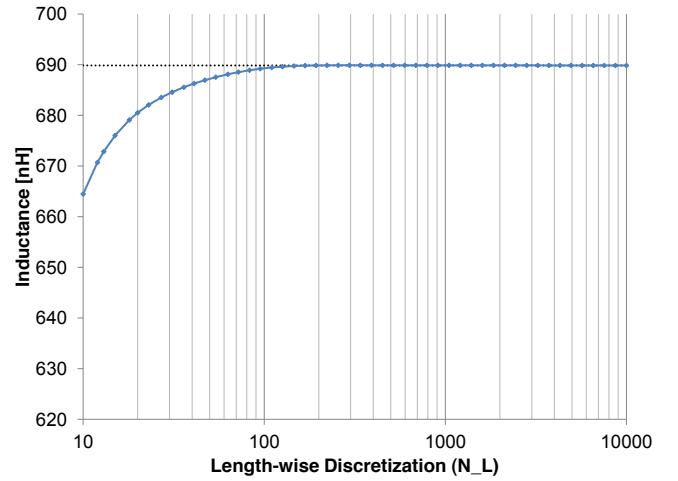
(a)

(b)

Figure 5: Convergence of free-space inductance for a single turn against closed-from solution from Grover [29]. The numerical results are generated using an N_L-sided polygon to approximate the ideal circle. (a) Inductances, (b) relative errors with increasing discretization.

confirm the ability of our method to accurately compute the self-inductance of a circular turn modeled using linear filaments, and suggest that a polygon with more than 200 sides is, within 5 significant figures, an accurate representation of a circle.

B. Skin-effect Resistance of a single turn in free-space

For an isolated wire of circular cross-section, the exact frequency-dependent ratio of its a.c. resistance to its d.c. resistance is known in closed form, derived by solving the cylindrically-symmetric diffusion equation using Kelvin functions [6], [50]. In this subsection, we again consider a single turn of 0.1m radius, but this time with a circular cross-section of 1 mm in diameter. The turn is approximated as a 100-sided regular polygon, and the cross-section is modeled to be

circular using the techniques previously shown in Fig. 2. The geometry yields exact a.c.-d.c. ratios of 1.006790 at 10 kHz, 1.449801 at 100 kHz, and 4.045194 at 1 MHz.

Figure 6 shows the convergence of the simulated frequency-dependent resistance ratio with increasing discretization of the conductor cross-section. At the coarsest discretization value of $N = 1$, the wire cross-section contains only a single piecewise constant filament of constant current density, and it is consequently unable to capture any a.c. resistance effects. However, as the cross-section is divided into more piecewise constant filaments, the resistance ratios quickly converge to analytical values. These results suggest that skin-effect prediction errors are heavily dominated by the ability of the piecewise constant basis functions to capture the non-uniform current density distribution. These results agree with previous attempts to model the skin-effect using PEEC, although the ability to accommodate for far more filaments have resulted in more accurate predictions [31].

### C. Added resistance and inductance of circular filaments

When a conductor, placed over or in between a multilayer media structure, is assumed to have a constant and uniform current density, its terminal impedance can be decoupled into four independent components:

$$Z_{term} = (R_0 + \Delta R) + j\omega(L_0 + \Delta L)$$

where R_0 and L_0 are the series resistance and inductance of the coil in free-space and ΔR and ΔL are the added resistance and inductance caused by the presence of the multilayer media. If the conductor can be approximated as an interconnected set of circular, concentric, zero-volume filaments, then the ΔR and ΔL portion of its terminal impedance can be written in closed-form in the Hankel spectral domain, and inverted to the spatial domain with a Sommerfeld integral [1], [20], [28], [51].

Consider the 28-turn coil experimentally verified below in Section VII, modeled as 28 concentric circular turns, approximated with thin linear filaments. The turns are set to be physically isolated from each other, but are numerically modeled as being "in series" during the impedance extraction. The cross-section of each turn is set to be a single piecewise-constant filament of only $10\mu m$ width and height, in order to approximate the ideal zero-volume filament. Like Section VII, we place the coil below a copper plate of 1/8th inch thickness. The analytical benchmark for ΔR and ΔL is taken from equations (13)-(15) of [28], and evaluated to machine precision using adaptive quadrature.

Figure 7 shows the convergence of the numerical method to the analytical benchmark with increasing fineness of the discretization. The Green's function and the pFFT algorithm are both tuned to 3-4 s.f. of accuracy. Results show convergence to this specified accuracy, accomplished by conforming to the necessary assumptions for the analytical derivations: a constant current density, a thin filament current, and perfectly circular turns.
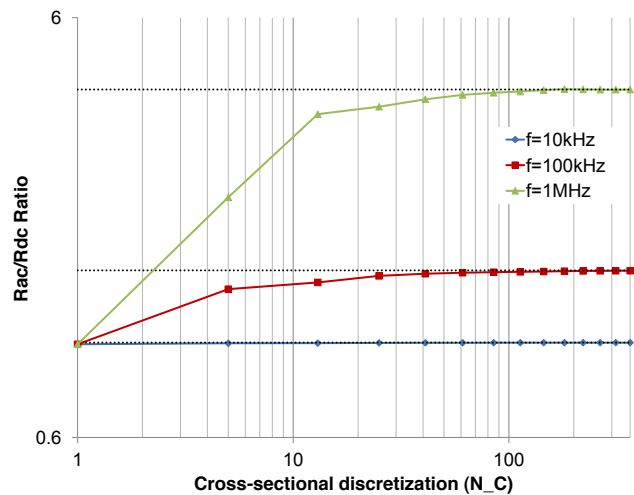
(a)
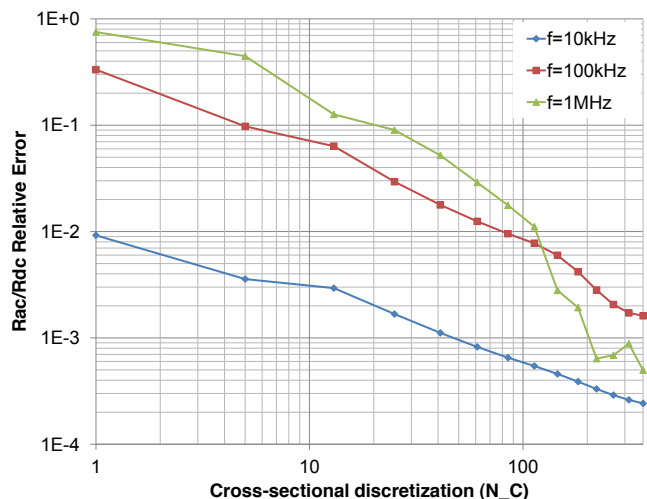
(b)

Figure 6: Convergence of skin-effect resistance for a single isolated turn against closed-from solution from McLachlan [50]. The cross-section is progressively refined with more filaments, each of constant current density. (a) A.c.-d.c. resistance ratios (b) relative errors with increasing discretization.

VII. EXPERIMENTAL VERIFICATION OF A LITZ WIRE COIL

The results above suggest that the numerical method can replicate the predictions made by analytical models given the same inputs and assumptions. Extending this result, we aim to demonstrate in this section that it can also make more accurate predictions, by working with a more faithful model of the system and making less assumptions.

To achieve this, we perform a series of experiments on a 28-turn, 16-strand litz wire induction heating coil, shown in Fig. 8. Two experimental cases are considered:

- The coil alone ("free-space case"),
- The coil placed underneath a flat 1/8 inch copper plate ("plate case").

These cases are specially chosen as accuracy benchmarks, because they can be exactly described at quasistatic frequen-
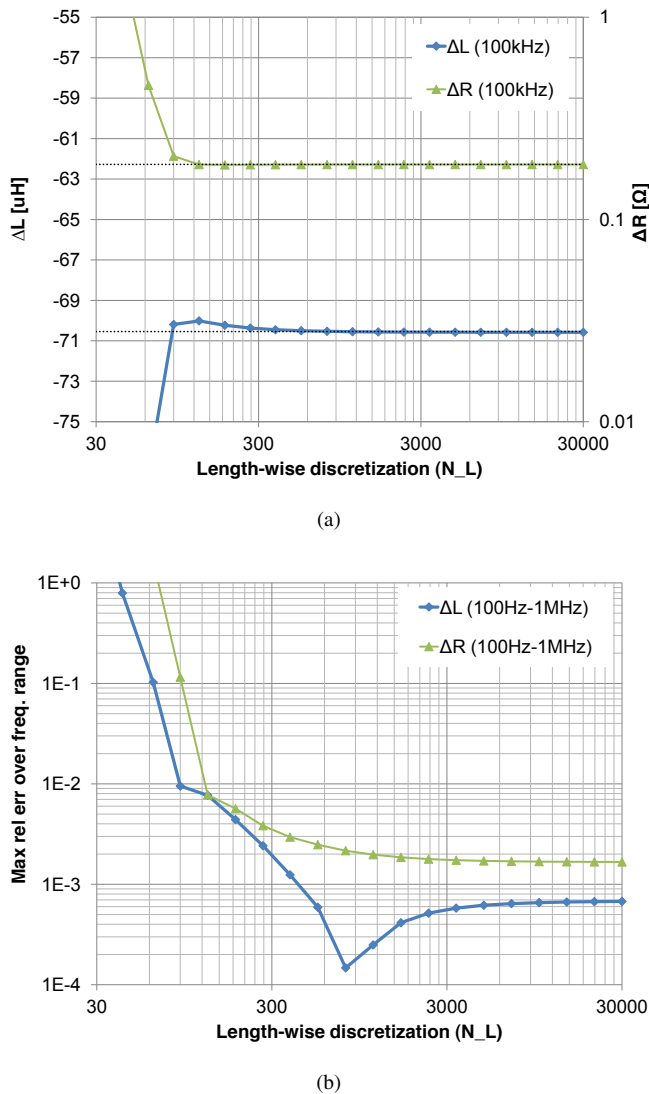
(a)

(b)

Figure 7: Convergence to the analytical $\Delta L/\Delta R$ models with refinement of the number of filaments N in numerical model. (a) Convergence of ΔL for 3 chosen frequencies. (b) Convergence of the maximum relative error (ΔL and ΔR) over 30 frequencies for a solid conductor numerical model and a zero-volume filament numerical model.

cies with the linear formulation presented in Section II. In other words, given a perfectly faithful model of the coil and plate geometries, prediction accuracy is limited only by the ability to solve the governing equations. Whereas for non-linear materials like steels and irons, a linear formulation is only approximate, and the prediction accuracy would be bound by the linearization process, i.e. the choice of $\mu_r = \mu_r' - j\mu_r''$.

In the following section, the impedance magnitude and phase measurements are made using an Agilent 4192A low-frequency impedance analyzer. Predictions of the coil series inductance L, resistance R, and quality factor $Q = \omega L/R$ are computed using the numerical method described above, and also using popular analytical formulas derived specifically for a circular coil in proximity to multilayered media.

A. Experimental setup and model description

The exact litz wire used in the experimental coil has a long and thin, tape-like cross-section, containing 16 strands of annealed copper wire with $\sigma = 5.8 \times 10^7$ S/m. The strands are wound in two layers of 8, in alternating angles of incline as shown in Fig. 9. The distance between the center of the first strand and the ninth strand is 23.72 ± 0.05 mm, at an angle of $17.5°$. The height of the tape is 7.49 ± 0.03 mm, and each strand of wire has a circular cross-section diameter of 0.80 ± 0.02 mm and negligible insulation thickness.

The turns of the coil are wound in three separate sections:

- 7 inner turns, tightly wound with outermost radius at 49.2 ± 0.4 mm.
- 9 middle turns, tightly wound with outermost radius at 82.6 ± 0.4 mm.
- 12 outer turns, tightly wound with outermost radius at 114.3 ± 0.4 mm.

The copper plate used comprises of 99.9% annealed copper, of 3.175 ± 0.013 mm thickness, $\mu = \mu_0$ and $\sigma = 5.80 \times 10^7$ S/m, and is placed 10.62 ± 0.02 mm over the top of the coil.

The numerical model for the coil was constructed in MAT-LAB, discretized it into 909,504 elements. Each element is a brick-shaped filament of 1mm in length and 0.1mm in width and height. The 16 strands are each modeled as a round wire, refined into 25 rectangular sub-filaments along its cross-section, according to the cosine rule previously illustrated in Fig. 2. It is worth emphasizing that the element count should not be directly compared with the finite element method. An equivalent finite element model for this system would discretize not only the conductor, but also the surrounding multilayered media and free-space, and increasing the element count by a factor of 20-200 [23]–[25].

Finally, the circular coil is well-known to yield accurate, analytical solutions for the multilayer media problem [1], [52]. As a final comparison, we make predictions of the series inductances using formulas from literature. The free-space inductance L_0 is computed using closed-form expressions in [29], [49], and the free-space series resistance R_0 of a litz wire coil wound with round wires is taken from proximity effect expressions derived by [6], [7]. Here, the fill-factor of the wire is taken to be the cross-sectional area of 16 strands of wire, divided by the cross-sectional area of the litz wire bundle: $16 \times \pi(0.8\text{mm}/2)^2/(7.5\text{mm} \times 1.6\text{mm}) = 0.67$. The added ΔR and ΔL terms are computed using expressions from [28].

B. Series inductance predictions

Before comparisons can be made, we note that a practical induction heating coil experiences parallel resonance due to its internal winding-to-winding capacitances. Experimental evidence suggests that this capacitance is approximately frequency-independent [2], [3]. By measuring the resonance frequencies to 2.636 MHz and 3.855 MHz for the free-space and plate cases respectively, we estimate the parallel terminal capacitance for the coil to be 30 ± 3 pF.

The raw terminal impedance measurements are compensated assuming 30 pF of capacitance, and compared to predic-
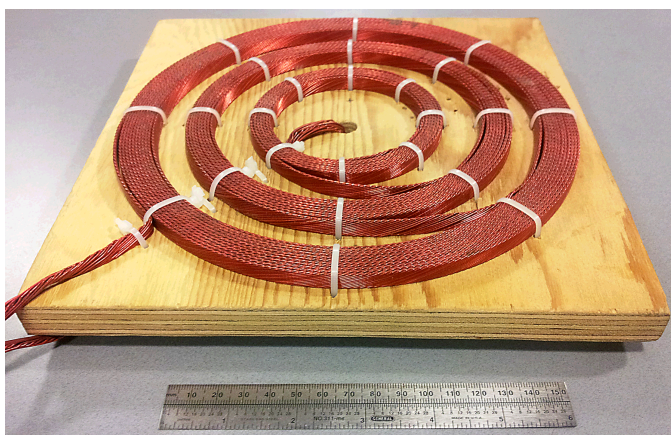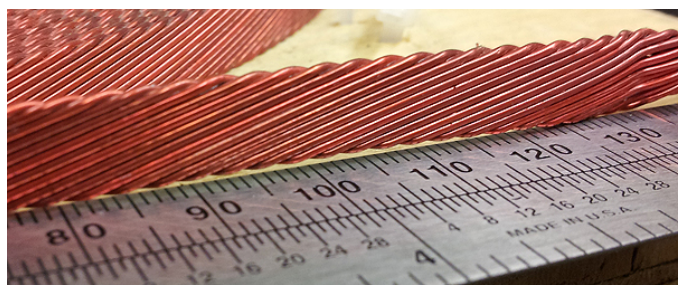
(a)
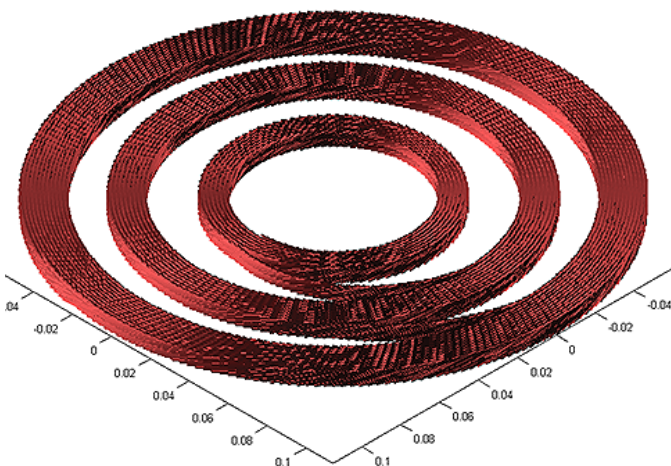
(b)

Figure 8: The example coil used in this paper: (a) actual coil; (b) discretized model.

(a)

(b)

Figure 9: Detailed image of litz pattern: (a) actual coil; (b) discretized model. Note that each strand is actually modeled with a circular cross-section. They are shown with square cross-sections here for clarity.

Table I: Capacitance compensated terminal impedance magnitude and phase measurements, compared to numerically simulated values.

Coil in free-space						
	Raw Meas.		Cap. Comp.		Simulated	
Freq.	$|Z|$	$\arg(Z)$	$|Z|$	$\arg(Z)$	$|Z|$	$\arg(Z)$
1 kHz	0.1341	73.09°	0.1341	73.09°	0.1349	72.40°
10 kHz	1.2843	86.38°	1.2843	86.38°	1.2879	86.24°
100 kHz	12.668	81.05°	12.648	81.06°	12.648	82.98°
1 MHz	142.75	83.44°	122.01	84.38°	123.24	86.08°

Coil below plate						
	Raw Meas.		Cap. Comp.		Simulated	
Freq.	$|Z|$	$\arg(Z)$	$|Z|$	$\arg(Z)$	$|Z|$	$\arg(Z)$
1 kHz	0.0842	45.52°	0.0842	45.52°	0.0829	46.71°
10 kHz	0.5980	76.56°	0.5978	76.65°	0.6036	76.13°
100 kHz	5.7689	71.08°	5.7632	71.14°	5.7787	71.16°
1 MHz	55.872	80.93°	52.382	81.39°	52.530	79.68°

tions made by the numerical model in Table I. The frequency-scaled, imaginary component of each terminal impedance (i.e. the "inductance" in an assumed series RL network) is plotted in Fig. 10. Results confirm the presence of an artifact resonant peak in the raw measurement, which is removed when the capacitive effects are compensated. The accuracy of the numerical predictions improves accordingly.
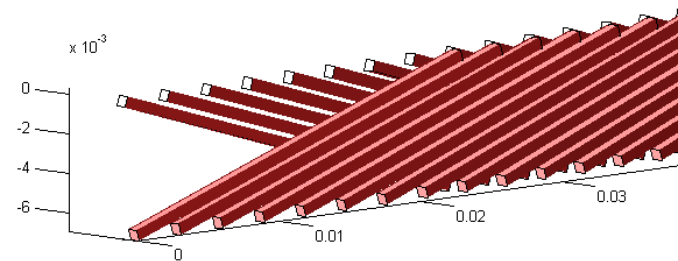
Figure 11 plots these same results compared against predictions made by the analytical models, zoomed and scaled to the relevant ranges. Results show that both methods are able to accurately predict the inductance to 3 significant figures at lower frequencies, but only the numerical method is able to maintain its accuracy at high frequencies. The presence of the plate causes eddy currents to be induced in the plate which in turn re-induces eddy currents within the wire bundle. This effect is fully captured in the numerical model.

C. Series resistance and quality factor predictions

Figure 12 compares the measured series resistance of the coil against predictions made by the numerical model and by the analytical model, and Fig. 13 plots the equivalent

comparison in the quality factor. The analytical fit is shown to be good until around 20 kHz, when current redistribution effects begin to dominate. Due to the complicated geometry of the litz winding, these loss effects are not well approximated by the analytical model beyond the initial knee frequency, and the maximum quality factors predicted are off by more than 10%. The numerical model is very accurate over its range of applicable frequencies, but begins to deviate from measurements at around 100 kHz. At this frequency, the skin depth of copper is 206.3 μm, around the same size as the cross-sectional width of the widest filament. Accuracy begins to deteriorate because the filaments become too large to fully capture the current density redistribution under the skin and proximity effects.
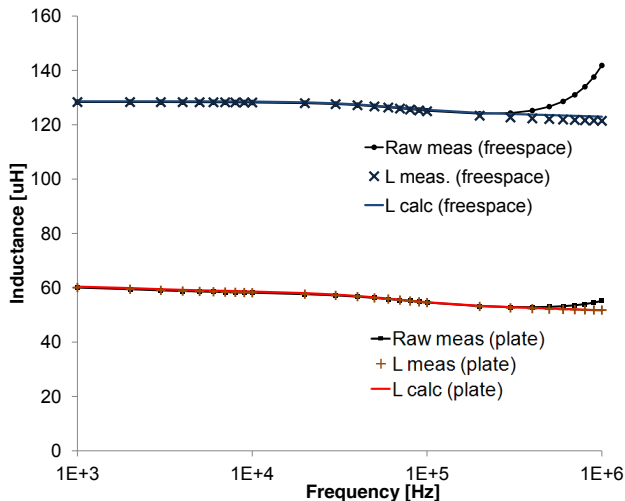
Figure 10: Coil inductance comparison of the frequency-scaled imaginary component of the terminal impedance ("Raw meas") with inductances measured assuming 30 pF of parallel capacitance ("L meas."), and inductances computed using the numerical method ("L calc").

The figures also show the predictions in the plate case. It is worth noting here that predictions made by the analytical model are considerably worse because it does not take into account the fact that some of the skin effect is actually canceled out by the presence of the plate, and that the series resistance measured is lower at very high frequencies than in the free-space case.

D. Predictions made without litz wire transpositions

To show that a full model of the litz wire transpositions is not superfluous for accurate predictions of the terminal impedance, we repeat the 11mm copper plate numerical simulations with a coil wound using a single solid conductor, in the shape of a long tape. We emphasize that this model approximates the litz wire as if it were untangled into a set of parallel strands, thereby eliminating its transposition patterns. The formulation and numerical method remain identical. In order to ensure that numerical discretization error does not artificially erode the accuracy of these simulations, the coil was discretized into 1,000,000 elements, 10,000 along its length and 100 along its solid cross section according a cosine rule.

Results for the tape, shown in Fig. 14, fit the measurements noticeably worse than the full litz wire model. Note that many characteristics of the tape conductor observed here have been previously described in literature, particularly the fact that the resistance of a solid conductor is actually lower than an equivalent litz wire at very high frequencies [6], [7].

E. Electric and magnetic fields

The electric field produced by the conductor is computed on a regular grid as a by-product of the pFFT algorithm. These fields can be separately extracted, and processed to compute the magnetic field, at no additional cost to the overall algorithm.
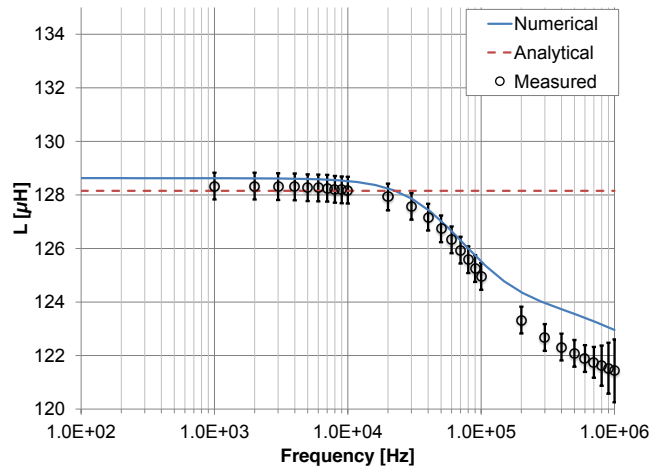

(a)
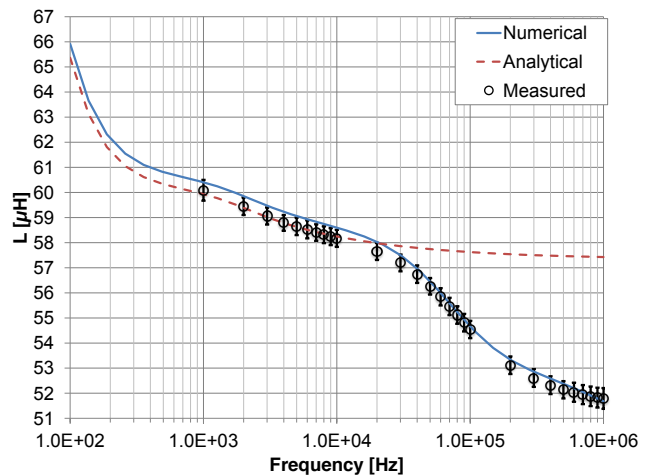
(b)

Figure 11: Coil inductance comparison, computed against measurements (b) in free-space and (c) with a plate over the coil. The measured inductance was extracted from raw measurements assuming 30 pF of parallel capacitance. Error bars show $\pm 0.4\,\mu H$ of measurement uncertainty, increasing to $\pm 1\,\mu H$ at higher frequencies due to uncertainty in the parallel capacitance.

VIII. Speed Comparison

Table II shows the computational time breakdown for the 30-point frequency sweep of the coil below the copper plate, using pFFT implemented in MATLAB, controlled to 0.1% relative error and run on a Intel Xenon 3.10 GHz 16-core workstation with 132Gb of RAM. The conductor geometry is discretized into 909,504 elements. We note that the simulation has also been performed on a 2.5 GHz dual-core laptop CPU in a similar amount of time to those shown, by using 10 times less elements and working to around 5% relative error.

The "fast pFFT" method is the procedure described in Section V, which avoids explicitly computing and precorrecting nearby interactions governed by G_{xx}^{add}. The grid was set up so
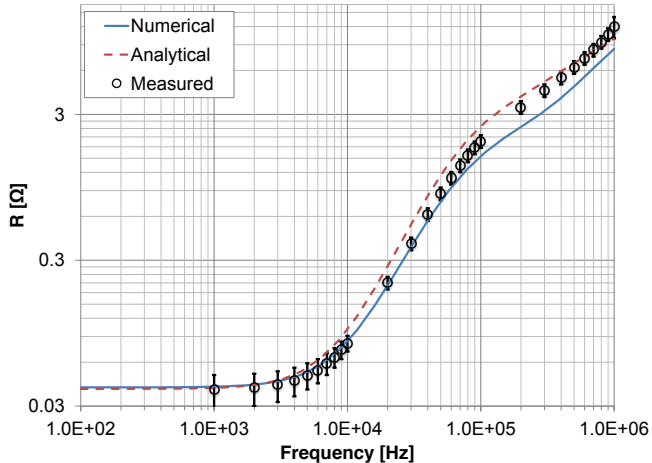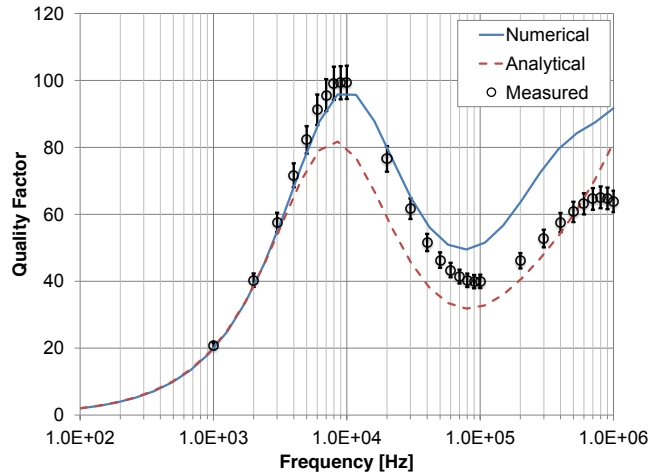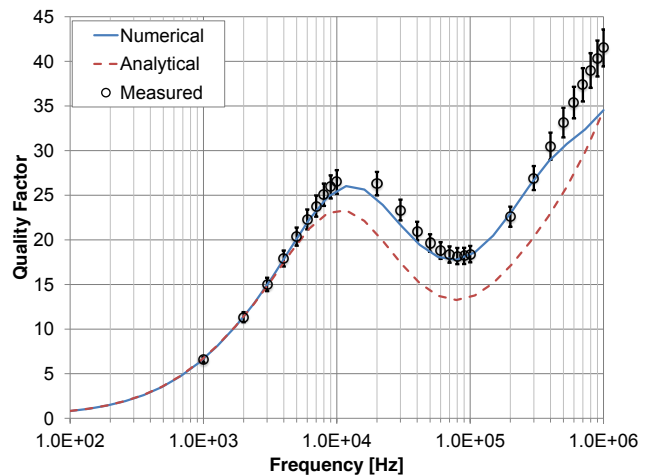
(a)
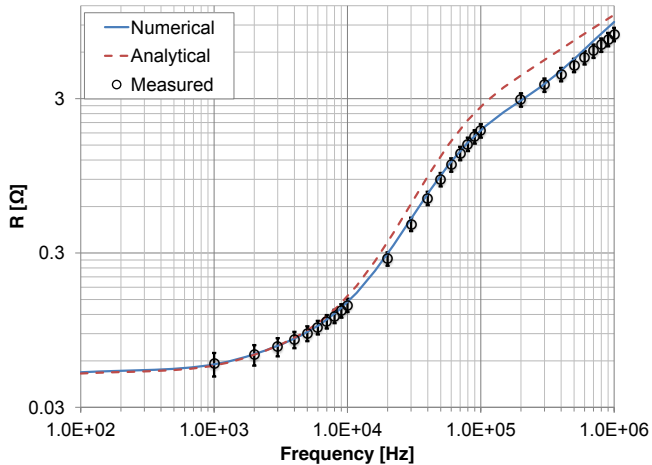
(b)

Figure 12: Coil series resistance predictions against measurements (after compensating for 30 pF of parallel capacitance) in the (a) free-space case and (b) the plate case. Error bars show $\pm 10\%$ of measurement uncertainty.

(a)

(b)

Figure 13: Coil quality factor predictions against measurements (after compensating for 30 pF of parallel capacitance) in the (a) free-space case and (b) the plate case. Error bars show $\pm 5\%$ of measurement uncertainty

that each cell is larger than the smallest conductor filament in the model, and resulted in 258×10^6 pairs of nearby interactions. These nearby interactions took a significant portion of time to compute, but was only performed once for the conductor geometry.

The "orig. pFFT" column illustrates the original pFFT implementation for ground-plane problems, as found in [12], [17]. Here, the nearby G_{xx}^{add} interactions are explicitly computed and precorrected at each frequency, taking up a bulk portion of the total computation time. The integration is performed using a six degree sparse grid Kronrod-Patterson quadrature with 257 quadrature nodes per interaction, to result in around 3 significant figures of accuracy [53]. We avoided the standard practice of expanding G_{xx}^{add} into a summation of G^{free} terms (such as implemented by [12]), because summing multiple interactions under G^{free} would be even more time consuming to compute. Despite the efficiency of the quadrature scheme,

the need to explicitly compute G_{xx}^{add} interactions at each frequency make the original pFFT algorithm more than five times slower than the fast pFFT method.

IX. CONCLUSIONS

Throughout this paper, a fast numerical method is presented for the simulation of a litz wire coil in proximity to a multilayer lossy-magnetic structure. By noting the fact that the governing Green's function is smooth for the given problem, we make full use of fast numerical methods based on polynomial expansions. We present a simple finite differences method to compute the Green's function, and show that the efficacy of a finite difference approximation leads directly to a fast frequency-sweep version of the precorrected FFT. This version of the pFFT avoids repeating the setup phase at each frequency, and is consequently over five times faster than the
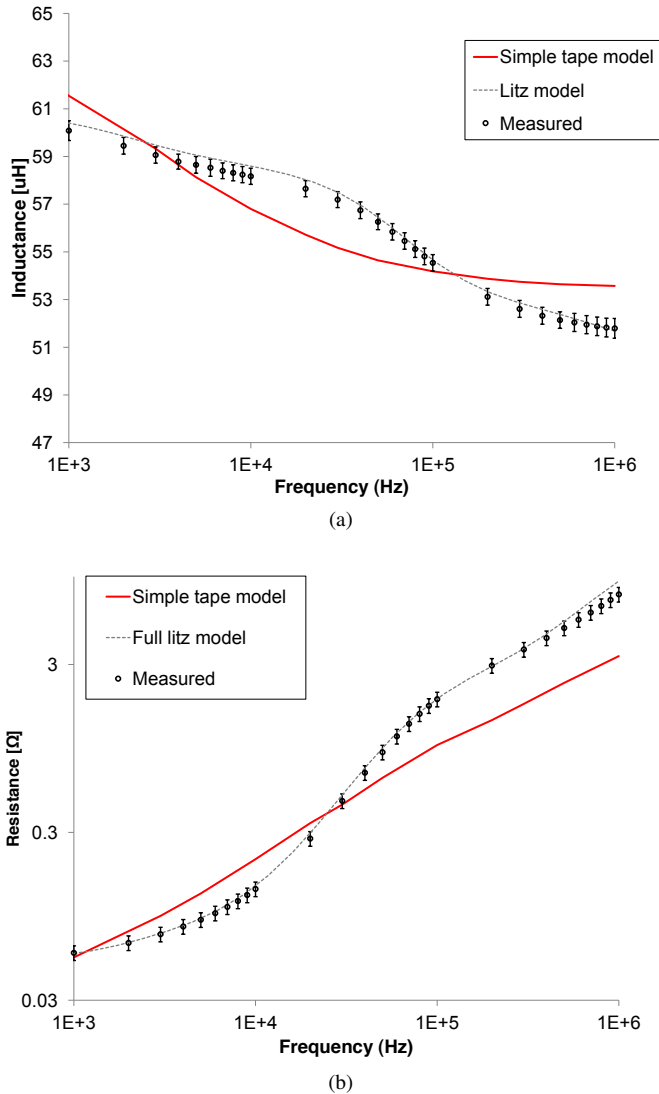
(a)

(b)

Figure 14: Simulating the litz wire with a solid conductor "tape" instead of a full litz structure, results in inductance and resistances that fit the measured values noticeably worse than the full litz-wire model described earlier. Results shown are for the plate case.

original pFFT method. Finally, we describe a numerical decomposition of the multilayer Green's function into a Toeplitz-plus-Hankel structure, which allows convolutions with it to be performed using the FFT. Experimental verifications are made for a 16-strand litz wire coil, realistically modeled down to each individual strand. Results are obtained in 2-3 hours on a workstation computer, showing an excellent agreement to measurements, including the subtle geometry-dependent characteristics not fully captured by less detailed models.

The source code for the work presented can be found online at http://web.mit.edu/ryz/www, or by emailing the corresponding author at ryz@mit.edu.

X. Acknowledgments

Table II: Computation time breakdown for the frequency sweep of a 28-turn coil, discretized to 909,504 elements, over 30 frequencies, controlled to 0.1% relative error.

	Fast pFFT		Orig. pFFT	
	per f	total	per f	total
Setup Geometry				
Grid size	$256 \times 256 \times 32$		$256 \times 256 \times 32$	
Projection[1]	-	9.7 s	-	(9.7 s)
Nearby Interactions				
Num. direct terms	258×10^6		258×10^6	
Precorrection[2]	-	209 s	210 s	(6309 s)
Direct G^{free} terms[3]	-	1545 s	-	(1545 s)
Direct G^{add} terms[4]	-	-	1341 s	(40248 s)
Extract Impedance				
Setup G^{add} kernel[5]	4.33 s	130 s	4.21 s	(130 s)
GMRES iterations	41×	1237×	(41×)	(1237×)
Time per iteration	5.8 s	5.8 s	5.8 s	(5.8 s)
Total time to solve	240 s	7206 s	(240 s)	(7206 s)
Total Time	245 s	9091 s	1796 s	49339 s

[1] Line 3 of Fig. 4.
[2] Line 4 of Fig. 4. Each precorrection takes $0.5\mu s$.
[3] Line 5 of Fig. 4. Each free-space interaction takes 0.2-$40\mu s$ to compute, depending upon the orientation of the filaments.
[4] Lines 8-9 of Fig. 4. Each added interaction takes $5.2\mu s$ to compute, from 257 quadrature points per interaction, and $0.02\mu s$ per quadrature point evaluation.
[5] Lines 8-9 of Fig. 4.

Appendix

A. Mutual inductances for non-Manhattan filament interactions

Volume-to-volume integrals of the free-space Green's function (9) is used to compute the mutual inductance term [33]. For each interacting pair of current filaments ϕ_1 and ϕ_2, the following integral is performed:

$$M = \int_{\phi_1} \int_{\phi_2} R^{-1} \, d\mathbf{r} \, d\mathbf{r}' \qquad (58)$$

where the spherical radius R is given:

$$R = \|\mathbf{r} - \mathbf{r}'\|.$$

The integration kernel becomes singular or close-to-singular when ϕ_1 and ϕ_2 are close or even overlapping. If ϕ_1 and ϕ_2 are brick-shaped and have their edges parallel to each other in the "Manhattan geometry", then closed-form solutions to (58) can be used to compute the mutual inductance [30].

When ϕ_1 and ϕ_2 are brick-shaped but non-Manhattan, e.g. at a slight angle to each other, then closed-form solutions to (58) do not exist. Instead, two of the six integral dimensions can be implicitly eliminated with a surface-to-surface transformation. As shown by [54], the $1/R$ kernel can be written as the divergence of a gradient:

$$R^{-1} = \frac{-1}{2} \nabla' \cdot \nabla R, \qquad (59)$$

and by the divergence theorem, (59) reduces (58) to a set of surface integrals with the spherical radius R itself as the

kernel:

$$M = \frac{-\hat{\mathbf{n}} \cdot \hat{\mathbf{n}}'}{2} \oint_{\partial\phi_1} \oint_{\partial\phi_2} R \, \mathrm{d}S \, \mathrm{d}S', \qquad (60)$$

where $\hat{\mathbf{n}}$ and $\hat{\mathbf{n}}'$ are the exterior normal vectors to the field surface $\mathrm{d}S$ and the source surface $\mathrm{d}S'$ respectively. For arbitrarily oriented cuboids basis functions, the above integral results in 36 surface-to-surface interactions:

$$M = \sum_{i=1}^{6} \sum_{j=1}^{6} \frac{-\hat{\mathbf{n}} \cdot \hat{\mathbf{n}}'}{2} \int_{\square_i} \int_{\square_j'} R \, \mathrm{d}S \, \mathrm{d}S', \qquad (61)$$

where $\square_1 \cdots \square_6$ and $\square_1' \cdots \square_6'$ are the six surfaces of the field and source cuboids respectively. Note that the surface-to-surface kernel, R, is no longer singular.

Through coordinate rotations, one of the two interacting surfaces of (61) can always be set to align with the $\hat{\mathbf{x}}$ and $\hat{\mathbf{y}}$ directions, such that $\mathrm{d}S \to \mathrm{d}x \, \mathrm{d}y$. Then, two of the four remaining integrals can be evaluated analytically, with the following identity:

$$\begin{aligned}
I(x,y,z) = \int \int & \sqrt{x^2 + y^2 + z^2} \, \mathrm{d}x \, \mathrm{d}y \\
= & \frac{xy\sqrt{x^2+y^2+z^2}}{3} \\
+ & \frac{y^3 + 3yz^2}{6} \log\left(\frac{x + \sqrt{x^2+y^2+z^2}}{\sqrt{y^2+z^2}} \right) \\
+ & \frac{x^3 + 3xz^2}{6} \log\left(\frac{y + \sqrt{x^2+y^2+z^2}}{\sqrt{x^2+z^2}} \right) \\
+ & \frac{z^3}{3} \mathrm{atan}\left(\frac{xy}{z\sqrt{x^2+y^2+z^2}} \right). \quad (62)
\end{aligned}$$

For example, suppose that the field rectangle, $\square_i$, is of length L and width W long the x and y directions respectively with one corner at the origin. Then, the inner two integrals of (61) is simply:

$$\begin{aligned}
\int_{\square_i} R \, \mathrm{d}S = & \, I(x', y', z') - I(x' - \mathrm{L}, y', z') \\
& - I(x', y' - \mathrm{W}, z') + I(x' - \mathrm{L}, y' - \mathrm{W}, z'). \quad (63)
\end{aligned}$$

The final two dimensions of integration over the source surface, $\square_j'$, are truly arbitrary, and should be evaluated numerically. Fortunately at this point, the remaining integrand $I(x,y,z)$ is so smooth that it can be integrated using any reasonable two-dimensional quadrature rule. In this paper, we have used a third-order two-dimensional Kronrod-Patterson quadrature rule with 9 nodes based on sparse grids [53].

REFERENCES

[1] W. Hurley and M. Duffy, "Calculation of self and mutual impedances in planar magnetic structures," *IEEE Transactions on Magnetics*, vol. 31, no. 4, pp. 2416–2422, Jul. 1995.

[2] A. Niknejad and R. Meyer, "Analysis, design, and optimization of spiral inductors and transformers for Si RF ICs," *IEEE Journal of Solid-State Circuits*, vol. 33, no. 10, pp. 1470–1481, 1998.

[3] ——, "Analysis of eddy-current losses over conductive substrates with applications to monolithic inductors and transformers," *IEEE Transactions on Microwave Theory and Techniques*, vol. 49, no. 1, pp. 166–176, 2001.

[4] S. Hui and W. Ho, "A new generation of universal contactless battery charging platform for portable consumer electronic equipment," *Power Electronics, IEEE Transactions on*, vol. 20, no. 3, pp. 620–627, 2005.

[5] J. Acero, J. Burdio, L. Barragan, D. Navarro, R. Alonso, J. Ramon, F. Monterde, P. Hernandez, S. Llorente, and I. Garde, "Domestic Induction Appliances," *IEEE Industry Applications Magazine*, vol. 16, no. 2, pp. 39–47, Mar. 2010.

[6] J. Ferreira, "Analytical computation of AC resistance of round and rectangular litz wire windings," *Electric Power Applications, IEE Proceedings B*, vol. 139, no. 1, pp. 21–25, 1992.

[7] J. Acero, R. Alonso, J. Burdio, L. Barragán, and D. Puyal, "Frequency-dependent resistance in litz-wire planar windings for domestic induction heating appliances," *Power Electronics, IEEE Transactions on*, vol. 21, no. 4, pp. 856–866, 2006.

[8] X. Nan and C. Sullivan, "An equivalent complex permeability model for litz-wire windings," *IEEE Transactions on Industry Applications*, vol. 45, no. 2, pp. 854–860, 2009.

[9] P. Dowell, "Effects of eddy currents in transformer windings," *Proceedings of the IEEE*, vol. 113, no. 8, pp. 1387–1394, 1966.

[10] J. Acero, P. Hernandez, J. Burdio, R. Alonso, and L. Barragdan, "Simple resistance calculation in litz-wire planar windings for induction cooking appliances," *Magnetics, IEEE Transactions on*, vol. 41, no. 4, pp. 1280–1288, 2005.

[11] R. F. Harrington, *Time-Harmonic Electromagnetic Fields (IEEE Press Series on Electromagnetic Wave Theory)*. Wiley-IEEE Press, 2001.

[12] T. Moselhy, X. Hu, and L. Daniel, "pFFT in FastMaxwell: a fast impedance extraction solver for 3D conductor structures over substrate," in *Proceedings of the conference on Design, automation and test in Europe*, vol. 1, no. 5. EDA Consortium, 2007, pp. 1194–1199.

[13] Y. Chow, J. Yang, D. Fang, and G. Howard, "A closed-form spatial Green's function for the thick microstrip substrate," *IEEE Transactions on Microwave Theory and Techniques*, vol. 39, no. 3, pp. 588–592, Mar. 1991.

[14] M. Aksun, "A robust approach for the derivation of closed-form Green's functions," *IEEE Transactions on Microwave Theory and Techniques*, vol. 44, no. 5, pp. 651–658, May 1996.

[15] K. Michalski and J. Mosig, "Multilayered media Green's functions in integral equation formulations," *IEEE Transactions on Antennas and Propagation*, vol. 45, no. 3, pp. 508–519, Mar. 1997.

[16] L. Greengard and V. Rokhlin, "A fast algorithm for particle simulations," *Journal of Computational Physics*, vol. 73, no. 2, pp. 325–348, Dec. 1987.

[17] J. Phillips and J. White, "A precorrected-FFT method for electrostatic analysis of complicated 3-D structures," *IEEE Transactions on Computer-Aided Design of Integrated Circuits and Systems*, vol. 16, no. 10, pp. 1059–1072, 1997.

[18] S. Kapur and D. E. Long, "IES 3 : a fast integral equation solver for efficient 3-dimensional extraction," *Proceedings of the 1997 IEEE/ACM international conference on Computer-aided design*, pp. 448–455, Nov. 1997.

[19] M. Bebendorf, "Approximation of boundary element matrices," *Numerische Mathematik*, vol. 86, no. 4, pp. 565–589, Oct. 2000.

[20] C. Dodd, "Analytical Solutions to Eddy-Current Probe-Coil Problems," *Journal of Applied Physics*, vol. 39, no. 6, pp. 2829–2838, 1968.

[21] H. A. Haus and J. R. Melcher, *Electromagnetic fields and energy*. Prentice-Hall, 1989.

[22] J. Shen, *Computational Electromagnetics Using Boundary Elements: Advances in Modelling Eddy Currents (Topics in Engineering)*. Computational Mechanics, 1995.

[23] O. Biro and K. Preis, "On the use of the magnetic vector potential in the finite-element analysis of three-dimensional eddy currents," *IEEE Transactions on Magnetics*, vol. 25, no. 4, pp. 3145–3159, Jul. 1989.

[24] A. Bermudez, C. Reales, R. Rodriguez, and P. Salgado, "Numerical analysis of a finite-element method for the axisymmetric eddy current model of an induction furnace," *IMA Journal of Numerical Analysis*, vol. 30, no. 3, pp. 654–676, Mar. 2009.

[25] O. Kanoun, *Lecture Notes on Impedance Spectroscopy: Measurement, Modeling and Applications*. CRC Press, 2012.

[26] J. Bowler, "Eddy current calculations using half-space Green's functions," *Journal of applied physics*, vol. 61, no. 3, pp. 833–839, 1987.

[27] J. Juillard and B. D. Barmon, "Simple analytical three-dimensional eddy-current model," *IEEE Transactions on Magnetics*, vol. 36, no. 1, pp. 258–266, 2000.

[28] W. Hurley and M. Duffy, "Calculation of self-and mutual impedances in planar sandwich inductors," *Magnetics, IEEE Transactions on*, vol. 33, no. 3, pp. 2282–2290, 1997.

[29] F. W. Grover, *Inductance Calculations: Working Formulas and Tables*, second edi ed. New York: Dover, 1962.

[30] C. Hoer and C. Love, "Exact inductance equations for rectangular conductors with applications to more complicated geometries," *Journal of Research of the National Bureau of Standards – C. Engineering and Instrumentation*, vol. 69C, no. 2, pp. 127–137, 1965.

[31] W. T. Weeks, L. L.-H. Wu, M. F. McAllister, and A. Singh, "Resistive and Inductive Skin Effect in Rectangular Conductors," *IBM Journal of Research and Development*, vol. 23, no. 6, pp. 652–660, Nov. 1979.

[32] A. Ruehli, "Equivalent Circuit Models for Three-Dimensional Multiconductor Systems," *IEEE Transactions on Microwave Theory and Techniques*, vol. 22, no. 3, pp. 216–221, Mar. 1974.

[33] A. E. Ruehli, "Inductance Calculations in a Complex Integrated Circuit Environment," *IBM Journal of Research and Development*, vol. 16, no. 5, pp. 470–481, Sep. 1972.

[34] M. Kamon, M. Ttsuk, and J. White, "FASTHENRY: a multipole-accelerated 3-D inductance extraction program," *IEEE Transactions on Microwave Theory and Techniques*, vol. 42, no. 9, pp. 1750–1758, 1994.

[35] Y. Saad and M. H. Schultz, "GMRES: A Generalized Minimal Residual Algorithm for Solving Nonsymmetric Linear Systems," *SIAM Journal on Scientific and Statistical Computing*, vol. 7, no. 3, pp. 856–869, 1986.

[36] J. Phillips, "Rapid solution of potential integral equations in complicated 3-dimensional geometries," Ph.D. dissertation, Massachusetts Institute of Technology, 1997.

[37] Z. Zhu, B. Song, and J. White, "Algorithms in FastImp: a fast and wide-band impedance extraction program for complicated 3-D geometries," *IEEE Transactions on Computer-Aided Design of Integrated Circuits and Systems*, vol. 24, no. 7, pp. 981–998, Jul. 2005.

[38] Z. Zhu, "Efficient techniques for wideband impedance extraction of complex 3-D geometries," Ph.D. dissertation, 2002.

[39] A. Niknejad, R. Gharpurey, and R. Meyer, "Numerically stable Green function for modeling and analysis of substrate coupling in integrated circuits," *IEEE Transactions on Computer-Aided Design of Integrated Circuits and Systems*, vol. 17, no. 4, pp. 305–315, 1998.

[40] D. Sitaram, Y. Zheng, and K. Shepard, "Full-chip, three-dimensional, shapes-based RLC extraction," *IEEE Transactions on Computer-Aided Design of Integrated Circuits and Systems*, vol. 23, no. 5, p. 711, 2004.

[41] W. Hurley and J. Kassakian, "Induction heating of circular ferromagnetic plates," *IEEE Transactions on Magnetics*, vol. 15, no. 4, pp. 1174–1181, Jul. 1979.

[42] V. Okhmatovski and A. Cangellaris, "A new technique for the derivation of closed-form electromagnetic Green's functions for unbounded planar layered media," *IEEE Transactions on Antennas and Propagation*, vol. 50, no. 7, pp. 1005–1016, Jul. 2002.

[43] A. G. Polimeridis, T. V. Yioultsis, and T. D. Tsiboukis, "Fast Numerical Computation of Green's Functions for Unbounded Planar Stratified Media With a Finite-Difference Technique and Gaussian Spectral Rules," *IEEE Transactions on Microwave Theory and Techniques*, vol. 55, no. 1, pp. 100–107, Jan. 2007.

[44] L. Hörmander, *Linear partial differential operators*, 3rd ed. New York: Springer, 1969.

[45] W. Milne, *Numerical solution of differential equations*, 1953.

[46] O. Nevanlinna, "Remarks on Picard-Lindelöf iteration," *BIT*, vol. 29, no. 2, pp. 328–346, Jun. 1989.

[47] B. Fornberg, "Calculation of Weights in Finite Difference Formulas," *SIAM Review*, vol. 40, no. 3, pp. 685–691, Aug. 1998.

[48] R. LeVeque, *Finite Difference Methods for Ordinary and Partial Differential Equations: Steady-State and Time-Dependent Problems (Classics in Applied Mathematic)*. SIAM, Society for Industrial and Applied Mathematics, 2007.

[49] T. Lyle, "On the self-inductance of circular coils of rectangular section," *Philosophical Transactions of the Royal Society of . . .*, 1914.

[50] N. McLachlan, *Bessel functions for engineers*. Oxford: Clarendon Press, 1955.

[51] J. Acero, R. Alonso, L. Barragán, and J. Burdio, "Modeling of planar spiral inductors between two multilayer media for induction heating applications," *Magnetics, IEEE Transactions on*, vol. 42, no. 11, pp. 3719–3729, 2006.

[52] J. Acero, R. Alonso, J. Burdio, L. Barragán, and D. Puyal, "Analytical equivalent impedance for a planar circular induction heating system," *Magnetics, IEEE Transactions on*, vol. 42, no. 1, pp. 84–86, 2006.

[53] F. Heiss and V. Winschel, "Likelihood approximation by numerical integration on sparse grids," *Journal of Econometrics*, vol. 144, no. 1, pp. 62–80, May 2008.

[54] L. Knockaert, "A General Gauss Theorem for Evaluating Singular Integrals over Polyhedral Domains," *Electromagnetics*, vol. 11, no. 2, pp. 269–280, Apr. 1991.